ELSEVIER

Composite Structures 52 (2001) 113–122

COMPOSITE STRUCTURES

www.elsevier.com/locate/compstruct

Analysis of an actively twisted rotor by multibody global modeling

Gian Luca Ghiringhelli, Pierangelo Masarati *, Paolo Mantegazza

Dipartimento di Ingegneria Aerospaziale, Politecnico di Milano, via La Masa 34, 20156 Milano, Italy

Abstract

The paper presents a procedure and the integrated tools for the aeroelastic analysis of an active twist helicopter rotor (ATR). The active twisting of rotor blades is carried out by induced-strain actuators distributed into the structure of the blade. Active fiber composites (AFC), made of piezoelectric fibers actuated by interdigitated electrodes (IDE), are used to obtain anisotropic induced-strain actuation capable of twisting the blade. The elastic, inertial and piezoelectric properties of the blade section are determined by a dedicated semi analytical formulation that accounts for the non-homogeneity and the anisotropy of the elastic and piezoelectric materials. A three-dimensional finite element analysis of the piezoelectric fiber with interdigitated electrodes is used to estimate the equivalent homogeneous material properties required for the blade section characterization. A four-blade, articulated rotor is analyzed in hover and forward flight conditions. The system is modeled by an original multibody formulation, implemented in a code named Multi-Body Dynamics (MBDyn). The equilibrium equations and the momenta are written for each body, together with the constraint equations, as a redundant coordinate set formulation. The blades are modeled as beam elements, by an original finite volume formulation for the analysis of nonlinear, initially curved and twisted beams subject to large displacements and rotations. The formulation is extended to include the effects of embedded piezoelectric devices as actuators. Electric and control-related degrees of freedom and elements have been added to MBDyn. Preliminary results related to the actuation authority of the active blade are presented.

Keywords: Active fiber composites; Active twist rotor; Beam analysis; Multi-body dynamics; Rotorcraft analysis

1. Overview

The work is presented in the following phases: (a) description of the need for induced twist in beam-like structures, and identification of the means to obtain it; (b) determination of the piezoelectric properties of an elementary cell, made of a portion of a single piezoelectric fiber between two adjacent electrodes, embedded in an epoxy matrix with reinforcing fiberglass; (c) determination of the properties of an equivalent piezoelectric material; (d) characterization of the section of a blade with embedded AFC actuators; and (e) dynamic analysis of the active blade in a suitable active twist rotor blade application.

2. Active twist control

The strain-induced twisting of a slender body, like a rotor blade, requires the capability of inducing shear strains in the beam section, that result in a global twist of the structure. A very promising material for distributed and embedded induced strain actuation has been found with piezoelectrics. The piezoelectric effect is represented by the capability of a material to produce an electric polarization when loaded, and, on the contrary, to strain when subject to an electric field. In usual notation [1], the linearized piezoelectric constitutive law is

$$\begin{Bmatrix} S \\ D \end{Bmatrix} = \begin{bmatrix} s^{(E)} & d^{\mathrm{T}} \\ d & \epsilon^{(T)} \end{bmatrix} \begin{Bmatrix} T \\ E \end{Bmatrix}, \tag{1}$$

where $S_{6\times1}$ and $T_{6\times1}$ are the strain and stress arrays, and $E_{3\times1}$ and $D_{3\times1}$ are the electric field and the electric displacement arrays. Piezoelectric devices for distributed induced strain applications are manufactured in two-dimensional laminae, to be applied on, or embedded into, the passive host structure. The usual implementation results in thin, thickness-wise (direction 3) polarized laminae, that show an isotropic behavior in their plane, thus being unable to induce the desired twisting. In fact, the shear strain in the plane of the piezoelectric lamina is

$$\gamma_{xs} = 2\cos(\alpha)\sin(\alpha)(S_1 - S_2), \tag{2}$$

* Corresponding author. Tel.: +39-02-2399-8365; fax: +39-02-2399-8334.

E-mail address: masarati@aero.polimi.it (P. Masarati).

0263-8223/01/$ - see front matter
PII: S0263-8223(00)00193-8

where s, a combination of the y and z axes, lies in the plane of the beam section, and x is the axis of the beam, while S_1 and S_2 are the principal strains in the plane of the piezoelectric in the material frame and α is the relative angle between the material and the beam reference frames, resulting in no shear when the two induced strains, S_1 and S_2, are equal, due to the plane isotropy of the material. An in-plane anisotropic piezoelectric material is required to obtain different electrically induced strains in directions 1 and 2. A very effective mean has been found by applying the fiber composite technology to the ceramic piezoelectric material, resulting in the active fiber composites (AFC, [2]). Previous research led to the development of the interdigitated electrodes (IDE) principle [3] as a useful means to induce anisotropic in-plane actuation. Different solutions can be formulated, ranging from the bonding of elongated strips of conventional piezoelectric material to the host structure, which represent a macroscopic scale implementation of the piezo fiber concept, to the use of interdigitated electrodes alone, which introduce the desired anisotropy in the electric field. The interdigitated electrodes are aligned in pairs of conductive strips on both the upper and the lower surfaces of the piezoelectric. The pairs of strips are alternately charged planewise, so that an alternate, in-plane electric field normal to the strips is generated. The piezoeletric material is initially polarized by means of the strips themselves during the manufacturing process. The resulting device exploits the main piezoelectric coupling coefficient (d_{11}), which is usually larger than the secondary ones (d_{12}, d_{13}) and opposite in sign $(d_{12}, d_{13} = -kd_{11}$, with $0.2 \leqslant k \leqslant 0.5)$; both the fibers and the polarization are in direction 1. When used in conjunction with AFC, the interdigitated electrodes can apply the control tension exactly in the direction of the fiber, thus completely decoupling the induced strain in the direction of the fiber from the strains in the other directions. The electrically induced strain is applied in the direction of the piezoelectric fibers only, resulting in a truly anisotropic actuation in the plane of the active ply. Eq. (2) shows that when the fibers are oriented 45° apart from the beam axis, and the two normal strains are equal in magnitude and of opposite sign, the maximal coupled axial-shear actuation of the ply is obtained; the axial actuation loads can be canceled by stacking the alternately charged active plies oriented 90° apart from each other.

3. Material characterization

Different techniques have been developed to predict the elastic properties of fibrous composite materials starting from the elastic properties of their components, namely the fibers and the matrix. Most of the analytical formulations rely on the introduction of an overall constraint tensor which can be obtained by solving a problem for a single cylindrical cavity in an anisotropic medium, and then by averaging the result to consider an arbitrary number of repetitive inclusions. Two examples of such approach are represented by the so-called "self-consistent" and the Mori–Tanaka methods. The topic is reviewed in [4], where extensions to the case of thermoelectroelastic materials have been proposed, as well as in [5,6]. Such models rely on the symmetry and the relative simplicity of analytically modeling a single, indefinitely long fibrous inclusion. The case of the AFC with IDE is far more complicated due to the peculiar geometry of the electrodes, that add a higher degree of complexity to the behavior of the material. A ply of AFC material is usually made of a single layer of piezoelectric fibers, bounded to two thin films that carry the electrode patterns. It represents a three-dimensional, discrete, repetitive structure both from the mechanical and the electric standpoint. As a consequence, the elastic and electric fields are fully three-dimensional and periodical, due to the repetitivity of the pattern of the fibers in direction 2 and of the electrodes in direction 1. The present technology allows to manufacture one-fiber thick plies of the order of 0.10 mm [2]. The granularity of the repetitive pattern is such that, from a macroscopic point of view, an equivalent, homogeneous orthotropic piezoelectric material is expected to exist, and to be able to capture the fundamental behavior of the AFC material. Here an attempt is made to predict the properties of such corresponding continuum, by conventional electroelastic finite element analysis (FEA). By exploiting the symmetry of the piezoelectric component, a finite portion of fiber, comprised between the centerlines of two rows of electrodes, is modeled by the commercially available Abaqus FEA code; the FE models are shown in Fig. 1. The figure refers to the circular section fiber presently investigated at MIT [2] and to the rectangular section fiber under investigation at NASA Langley Research Center (LaRC) [7]. The latter geometry seems to be more promising in terms of ease of manufacturing, accuracy in bonding the IDEs to the fibers, and homogeneity of properties. The fiber is made of raw piezoelectric material (presently Morgan Matroc PZT-5H is being used at MIT's Active Materials and Structures Laboratory [8]). The circular fiber, manufactured by CeraNova Corp., has a 0.13 mm diameter, and dimensions smaller than 0.10 mm are expected soon; the rectangular fiber, obtained by cutting monolithic ceramic sheets, can be manufactured down to 0.13×0.07 mm^2 sections [9]. The piezoelectric properties of the specimen are determined by imposing one by one the boundary conditions pertaining to each independent strain and electric field conditions (i.e. the three unit extensions, the three unit shear deformation conditions, and the condition of unit electric field between two electrode sets) and computing the stress resultants. All

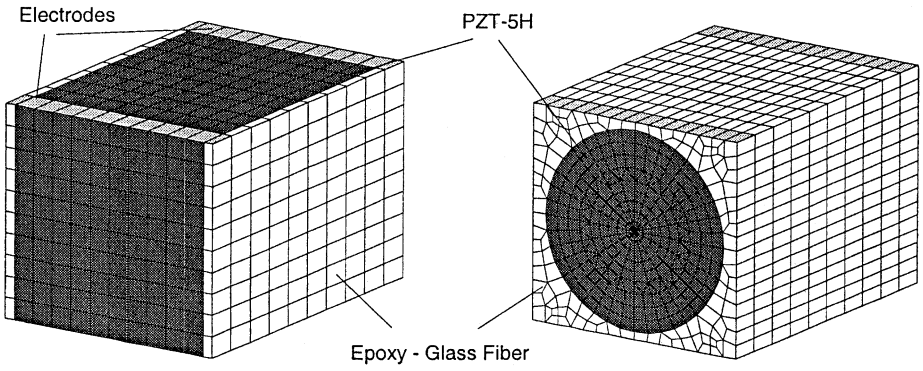

Fig. 1. FE models of the two specimens.

Table 1
Equivalent material properties

Property	Circular	Circular[a]	Rectangular
C_{11} (MPa)	71.7e + 3	82.5e + 3	83.5e + 3
C_{12} (MPa)	7.9e + 3	7.0e + 3	14.8e + 3
C_{13} (MPa)	8.6e + 3	7.5e + 3	20.2e + 3
C_{22} (MPa)	24.4e + 3	24.5e + 3	42.4e + 3
C_{23} (MPa)	6.7e + 3	6.9e + 3	15.6e + 3
C_{33} (MPa)	26.7e + 3	26.8e + 3	56.1e + 3
C_{44} (MPa)	3.5e + 3	3.5e + 3	5.6e + 3
C_{55} (MPa)	16.9e + 3	16.9e + 3	19.3e + 3
C_{66} (MPa)	8.1e + 3	8.1e + 3	11.4e + 3
e_{11} (C/m^2)	8.344	0.114	18.3
e_{12} (C/m^2)	−0.674	−0.009	−3.0
e_{13} (C/m^2)	−0.907	−0.012	−4.5

[a] No contact between the electrode and the piezoelectric fiber.

these boundary conditions are required because the beam-section analysis discussed later is based on the full three-dimensional properties of the material. The resulting properties of the equivalent materials are reported in Table 1. Figs. 2 and 3, respectively, show the Von Mises stress due to the unit axial strain applied to the clamped and close-circuit specimen and the detailed electric field due to the unit mean electric field applied to the electrodes of the completely clamped specimen.

4. Blade section characterization

The beam model is very commonly used to represent flexible rotor blades. Apart from its ease of implementation and use, it is able to describe the global behavior of the blade with a good trade-off between accuracy and demand of computational resources when nonlinear dynamics simulations are addressed. Moreover, it naturally couples with the strip theory used to model the aerodynamic forces, which considers the blade section as rigid from the aerodynamic standpoint. A more sophisticated structural model would involve a fully three-dimensional modeling of the displacement field, which in turn requires an aerodynamical model with a more detailed spatial resolution, at least two-dimensional panel methods, which radically increase the computational effort required for the analysis.

A beam model requires the knowledge of the elastic and piezoelectric properties of the passive and active parts of the active twist blade section; they are the constitutive matrices of linear piezoelectricity that express the internal forces and moments at each section of the beam as functions of the strains, the curvatures and the electric tensions on the electrodes. In the literature, these properties are usually estimated from the geometry

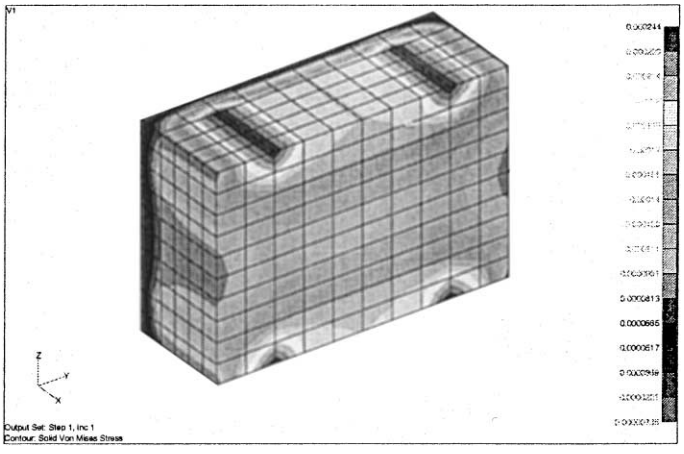

Fig. 2. Von Mises stress due to unit axial strain in rectangular fiber.

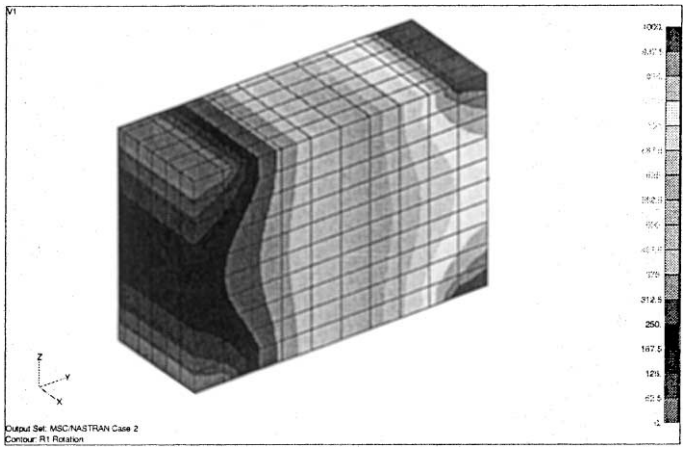

Fig. 3. Electric field due to unit voltage between the electrodes in rectangular fiber.

of the structural part of the beam section, such as the area, the second-order moments, and the polar moment in the principal reference frame of the section [10]. This approach is valid for a very first approximation computation, and can lead to poor estimates of the stiffness properties when anisotropic materials are considered. In case of hollow, thin-walled beam sections, interesting results can be obtained by generalizing the semi-monocoque model to the analysis of piezoelectric sections; an interesting example is represented by [11], where such a formulation is specialized to the analysis of multicell configurations. A more general and refined approach to the characterization of the section of an anisotropic, non-homogeneous beam has been used in the present paper. It is based on an original formulation [12,13] that has been extended to the analysis of beams embedding piezoelectric inclusions [14,15]. It relies on a two-dimensional finite element discretization of the section, that gives the user a great flexibility in the choice of the level of detail to be used in the characterization. The displacements $S_{3\times1}$ at an arbitrary point $f_{3\times1} = [0, y, z]^{\mathrm{T}}$ of the section are expressed as the combination of a warping displacement $g_{3\times1}$, superimposed to a reference rigid displacement and rotation of the whole section: $s = v(x) + g(x, y, z)$, where $v = Zr$ is the reference displacement, $Z_{3\times6} = [I_{3\times3}, -f\times]$ is a linearized rotation–translation matrix, and $r_{6\times1}$ are the displacements and the rotations of the reference point of the section. The strains $S_{6\times1}$ at an arbitrary point depend on both the reference and the warping displacements. While the reference displacements are functions of the position along the beam axis x only, the warping displacements depend also on the position in the beam section. The generalized deformations of the beam, $\psi_{6\times1}$, are expressed as functions of the derivatives of the reference displacements, i.e. $\psi = r_{/x} + \Pi r$. The matrix $\Pi_{6\times6}$ adds the contribution of the section rotation to the shear strain, i.e.

$$\Pi = \begin{bmatrix} 0_{3\times3} & e_x\times \\ 0_{3\times3} & 0_{3\times3} \end{bmatrix},$$

where e_x is the unit vector in the direction of the beam axis, x. The warping displacement contribution to the strains is hidden in the section characterization procedure. The warping displacements relax the overconstrained reference displacements that are rigid in the plane of the section. This relaxation, in usual beam formulations, is accounted for by transforming the three-dimensional material properties into a uniaxial stress state; this naturally accounts for the unloaded side-surface boundary conditions in the axial and bending load cases, while the torsion and the shear load cases usually require geometry-dependent adjustments to account for internal compatibility and for boundary conditions, resulting in a roughly approximated, geometry-based description of the effects of the warping. In case of non-homogeneous beam sections, the equilibrium and compatibility conditions must be enforced also at the boundaries between different materials, while in case of anisotropic materials, the strains due to a uniaxial stress state are fully coupled and imply a non-trivial warping solution. In this case, the usual beam characterization formulations fail even in the simple cases of axial and bending loads. In the present formulation, the warping displacements are discretized in a finite element way by means of arbitrary shape functions that describe the displacements in terms of their nodal value; the nodal displacements retain the dependency on the axial abscissa: $g = N_{3\times3n}(y, z)u_{3n\times1}(x)$. The electric potential V, which plays the role of the electric unknown, is described by analogy with the warping by means of the same shape functions: $V = N_{1\times n}(y, z)\ \varphi_{n\times1}(x)$. The discretized strain and electric fields are

$$S = \partial_{\mathrm{S}}(\psi, u, u_{/x}), \quad E = \partial_{\mathrm{E}}(\varphi, \varphi_{/x}),$$

where as $\partial_S(\cdot)$ and $\partial_E(\cdot)$ are two linear differential operators. The virtual work principle, generalized to include the electric work made by charging the piezoelectrics, is used; the domain of integration is shown in Fig. 4. The electric and the structural domains are not required to coincide, i.e. the host structure usually does not belong to the electric domain unless its dielectric properties are to be considered; the integration is intended to be performed only where the integrand fields are defined. The internal work per unit length is

$$\delta L_{i/x} = \int_A \left(\delta S^{\mathrm{T}} T + \delta E^{\mathrm{T}} D\right) \mathrm{d}A, \tag{3}$$

where T and D are the stresses and electric displacements from Eq. (1). The external work is made of an electromechanical contribution that represents the transmission of the internal forces and of the dielectric displacement along the beam, i.e. the work made by the stresses and the dielectric displacement on the two surfaces obtained by cutting the infinitesimal slice of beam

$$\delta L_{t/x} = \frac{\partial}{\partial x}\left(\int_A (\delta_s^{\mathrm{T}} p + \delta V^{\mathrm{T}} q)\, \mathrm{d}A\right) \tag{4}$$

being $p = T \cdot e_x$, $q = D \cdot e_x$ the stresses and the dielectric charge on the surface normal to the x-axis. An external contribution comes from the work made by the polarization charge on the electrodes of the piezoelectric devices

$$\delta L_{e/x} = \int_{\mathrm{c}} \delta V^{\mathrm{T}} q_{\mathrm{p}}\, \mathrm{d}l, \tag{5}$$

where q_{p} is the polarization charge per unit length that is imposed on the electrodes c. The actual electric field in the AFC with IDEs varies along the fiber in an alternate manner, as shown in Fig. 3, as the polarization direction does, but the averaged actuation behavior is that of a uniformly polarized piezoelectric material subject to an in-plane constant electric field in direction 1 (material frame). The correct material behavior is obtained by using the averaged material properties from the FEM analysis, while the effect of a constant electric field in direction 1 is obtained by applying a tension across the constant thickness of the piezoelectric plies (direction 3 in the material frame) and by switching the rows 1 and 3 of the piezoelectric matrix, $e = ds^{(E)^{-1}}$, of the AFC material. By carrying out the differentiations in Eq. (4), by

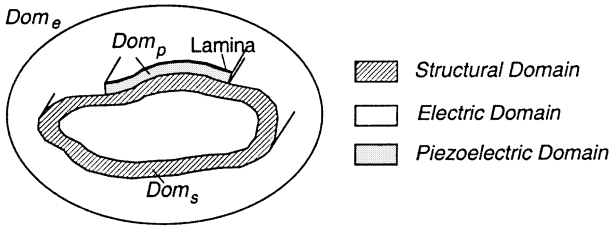

Fig. 4. Beam section.

equating the internal and external work expressions, Eq. 3 and Eqs. 4 and 5, respectively, and by operating some basic differentiations, the virtual work balance results in a second-order differential equation of the form

$$M_2 d_{/xx} + M_1 d_{/x} + M_0 d = F, \tag{6}$$

where $d = \{u, \varphi, \psi\}^{\mathrm{T}}$ are the unknown nodal warpings and voltages and the generalized deformations of the sections. Matrices M_0, M_1 and M_2 result from a standard finite element integration and assembly procedure. Their expressions are not reported for the sake of conciseness; the interested reader should consult Refs. [15,16]. The right-hand term, F, contains the internal forces in the section under analysis, and the polarization charge densities on the conductive laminae, namely $F = [0, Q_{\mathrm{c}}, \vartheta]^{\mathrm{T}}$. By assuming constant polarization charge densities and indicial internal forces, with linear bending moments resulting from the constant transverse shears, i.e.

$$F = \begin{Bmatrix} 0 \\ Q_0 \\ (I_{6\times 6} + x\Pi^{\mathrm{T}})\vartheta_0 \end{Bmatrix} = \left(\begin{bmatrix} 0 & 0 \\ 0 & I \\ I & 0 \end{bmatrix} + x \begin{bmatrix} 0 & 0 \\ 0 & 0 \\ \Pi^{\mathrm{T}} & 0 \end{bmatrix}\right) \begin{Bmatrix} \vartheta_0 \\ Q_0 \end{Bmatrix} = (H_0 + xH_1)\Theta_0.$$

Eq. (6) can be solved in terms of linear influence coefficients related to unit internal forces at $x = 0$, ϑ_0, together with an analogous solution due to unit polarization charges, Q_0, yielding

$$d_s = (d_{0s} + x d_{1s})\vartheta_0,$$
$$d_e = d_{0e} Q_0$$

or

$$d = (d_0 + x d_1)\Theta_0. \tag{7}$$

Fig. 5 shows the FEM model of the NACA 0012 airfoil that has been used in this analysis, while Fig. 6 refers to the warping due to different mechanical and electric load conditions of the blade section under analysis. Mention should be made of the electric boundary conditions for the linear term of the structural solution: the electric potential on the conductors must be constant along the beam axis, thus a non-holonomic constraint on the axial derivatives of the tensions must be introduced, as highlighted in [15]. The elastic and piezoelectric properties are obtained by substituting the solution, Eq. (7), evaluated at $x = 0$, into the expression of the internal work, Eq. (3), written in the form of Eq. (6), resulting in

$$\begin{aligned} \delta L_{i/x} &= \delta d^{\mathrm{T}}(M_1 d_{/x} + M_0 d) \\ &= \delta\Theta_0^{\mathrm{T}} d_0^{\mathrm{T}}(M_1 d_1 + M_0 d_0)\Theta_0 \\ &= \delta\Theta_0^{\mathrm{T}} \mathscr{C} \Theta_0, \end{aligned}$$

where the generalized piezoelectric compliance matrix of the section, $\mathscr{C}$, is introduced; its inverse is the piezo-

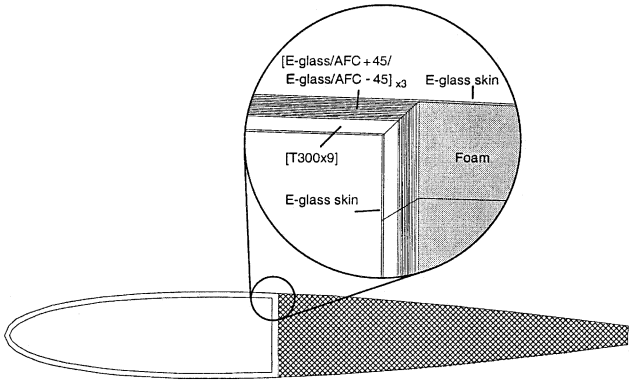

Fig. 5. Sketch of the blade section, with detail of the plies in the spar.

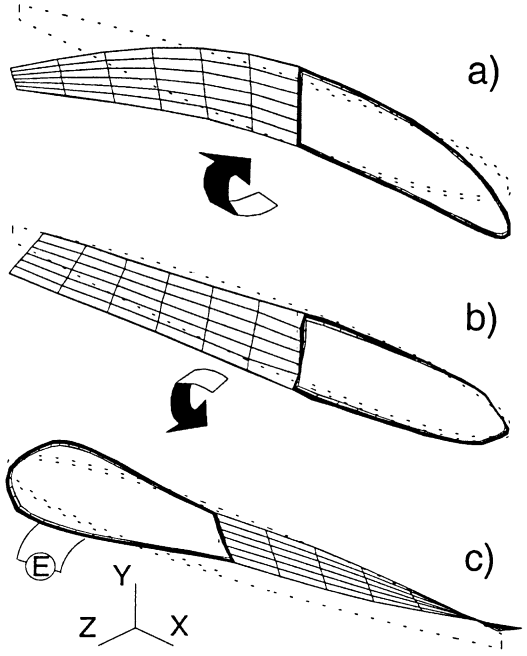

Fig. 6. Warpings due to: (a) out-of-plane bending; (b) torsion; (c) electric voltage that induces twist.

electric stiffness matrix $\mathscr{D} = \mathscr{C}^{-1}$. It can be decomposed in a 6×6 stiffness matrix K that in case of arbitrarily anisotropic, non-homogeneous materials will be fully coupled, an $N_e \times 6$ piezoelectric coupling matrix θ, N_e being the number of independent electrodes, and an $N_e \times N_e$ dielectric matrix. These matrices can be used in classical finite element beam/truss analysis codes. In this paper, a finite volume formulation, implemented in a multibody, nonlinear dynamics code, has been used [16–19].

5. Multibody active rotor analysis

The detailed analysis of a helicopter rotor requires the ability to thoroughly describe the kinematics of finite, and possibly large, displacements and rotations. The traditional approach is based on dedicated comprehensive codes, that usually make some simplifying basic assumptions, such as considering the blade motion as the superimposition of local rigid rotations about the rotor hinges and of local flexible linear displacements, expressed in modal form, onto the rigid rotation, possibly at constant velocity, of the rotor. This approach is valid, efficient in terms of computational speed and cost, and it is surely able to describe the fundamental behavior of the rotor; it can suffer from some limitations in case large rotations, nonlinear elastic behavior or non-uniform rotation conditions are to be addressed. In this paper a rather different approach has been used, based on a multibody description of the whole rotor. No assumptions are made on the kinematics of the components of the rotor. The model is divided into independent bodies, that carry the lumped inertia of the system. The six equilibrium equations are written for each body in the global reference frame; the bodies are constrained by kinematic constraints and by flexible elements that introduce configuration-dependent forces. The kinematic constraints are accounted for by adding the algebraic constraint equations to the system, and by introducing the constraint reactions as unknowns in the form of Lagrangian multipliers. Time integration is performed by an implicit, second-order accurate, linear multistep integration formula that is unconditionally stable and allows the control of the algorithmic dissipation [18]. The rotor blades are modeled by finite Volume C^0 beams [17,19]; strip theory with dynamic stall, radial flow and Mach correction is used, in conjunction with dynamic inflow modeling [20]. As discussed in [18,21], this approach allows a detailed analysis of the kinematics and of the dynamics of a rotorcraft avoiding any undue approximation in the kinematics of the system, and with the same order of refinement of a finite element model in the description of the flexibility, with reasonable and acceptable computational cost. The aerodynamic model is not as sophisticated as the structural one is, though it is acceptable for most applications, and will be the object of further development.

5.1. Numerical results

5.1.1. Model description

The numerical analysis is based on an analytical model of the active twist rotor presented in Ref. [7]. This is the analytical benchmark full-scale helicopter rotor the NASA Langley Research Center ATR wind tunnel model [22,23] refers to. It is representative of a large class of medium weight helicopter rotors. The basic properties of the rotor are described in Table 2. Two analytical models have been studied in this paper. The first one uses the same elastic and piezoelectric coeffi-

cients described in Ref. [7], for direct comparison and model validation purposes. The second model is based on the proposed blade section characterization method. The numerical results cannot be considered completely representative of the actual setup of the NASA ATR model, because the final active twist fitting of the ATR model is still under refinement. The presented results should be considered a sample application of the proposed analysis procedure. Table 3 presents the structural properties resulting from this analysis compared to those given in Ref. [7]; three increasingly refined meshes have been considered. The properties in Table 3 converge very quickly to their final value; the most challenging term is the position of the shear center, that travels from negative to positive as the mesh is refined. Further analyses with finer meshes confirmed that the presented value has converged to the final value. The AFC with rectangular fiber described in Table 1 has been used. The other materials used, namely ±45° fiberglass (E-glass) for the outer skin and between the piezoelectric plies, and T300 unidirectional graphite–epoxy for the inner part of the spar, are described in Table 4. The spar laminate has been obtained by stacking, from the inner side, a ply of fiberglass, followed by nine plies of T300 and by three sets of substacks made of fiberglass, +45° AFC, fiberglass and −45° AFC. A final ply of fiberglass has been used to wrap the whole section, including the trailing part, that has been filled with non-load carrying foam; a schematic is shown in the detail of Fig. 5. The thicknesses of the single plies are reported in Table 4. The spar goes from the leading edge to 40% of the blade chord; the piezoelectric plies are applied on the top and bottom surfaces approximately from 5% to 40% of the chord; in the web and in the nose the fiberglass is used instead of the AFC. The full stiffness and piezoelectric matrices obtained with the most refined mesh are reported in Table 5.

Table 2
Rotor geometric and dynamic properties (Ref. [7])

Symbol	Property	baseline	AFC blade
R	Blade radius	8.53 (m) 336 (in)	(same)
Ω	Rotation speed	22.25 (rad/s)	(same)
m	Section mass	7.65 (kg/m) 1.11e − 3 (lb s^2/in./in.)	7.10 (kg/m) 1.03e − 3 (lb s^2/in./in.)
c/R	Nondimensional chord	0.0488	(same)
θ_1	Linear pretwist	−8 deg/R	(same)
γ	Lock number	9.77	(same)

Table 4
Material and laminae properties

Property	Glass–epoxy	Graphite–epoxy
c_{11} (MPa)	14.8e + 3	181.8e + 3
c_{12} (MPa)	1.3e + 3	2.9e + 3
c_{22} (MPa)	13.7e + 3	10.3e + 3
c_{66} (MPa)	1.9e + 3	7.2e + 3
ρ (kg/m^3)	1.8e + 3	1.6e + 3
Thickness[a] h (mm)	0.130	0.125

[a] The thickness of the AFC plies is 0.140 (mm).

6. Model validation

The benchmark active twist rotor model of Ref. [7] has been implemented. The analytical model consists of the hub, a rigid body rotating at constant speed with respect to the ground; this carries the hinges of the four blades. Coincident hinges for flap and lag are used, at $0.027R$ from the rotation axis. A pitch bearing is placed just outward each hinge. The flexible blades are modeled by four three-node beam elements, with lumped inertia. The swashplate model contains: (a) scissors to prevent the relative rotation about the rotor axis between the fixed plate and the ground, and between the rotating plate and the hub; (b) the three variable distance actuators from the ground to the fixed plate; and (c) fixed distance links from the rotating plate to each blade to impose the blade pitch. The model was validated from a

Table 3
Stiffness properties (rectangular fiber)

Stiffness	Mesh 1	Mesh 2	Mesh 3	Ref. [7]
Axial (N)	7.96e7	8.23e7	8.27e7	n.a.
Shear in plane (N)	8.14e6	8.05e6	7.96e6	n.a.
Shear out of plane (N)	1.10e6	9.16e5	8.72e5	n.a.
Twist (Nm^2)	1.22e4	1.16e4	1.14e4	1.08e4
Bending out-of-plane (Nm^2)	2.85e4	2.92e4	2.94e4	3.79e4
Bending in-plane (Nm^2)	2.22e5	2.45e5	2.51e5	n.a.
Axial force center (% chord)	2.28	2.79	2.96	0.00
Shear center (% chord)	−1.68	1.26	2.18	0.00
Nodes	175	362	662	–
Elements	162	336	618	–

Table 5
Stiffness and piezoelectric matrices, ref. 25% chord. Units: N, m and V

	Axial	Shear		Twist	Bending	
		In-plane	Out-of-plane		In-plane	Out-of-plane
Axial	8.27e + 7	0.00e + 0	8.50e + 2	1.77e + 2	0.00e + 0	−3.11e + 5
Shear in-plane		7.96e + 6	0.00e + 0	0.00e + 0	−3.08e + 1	0.00e + 0
Shear out-of-plane			8.72e + 5	2.42e + 3	0.00e + 0	−1.31e + 2
Twist				1.06e + 3	0.00e + 0	−3.25e + 0
Bending out-of-plane		Sym.			2.73e + 3	0.00e + 0
Bending in-plane						2.33e + 4
Piezo	0.00e + 0	0.00e + 0	5.74e − 1	7.69e − 2	0.00e + 0	0.00e + 0

dynamic standpoint by comparing the in vacuo rotating frequencies to those presented in Ref. [7]. The frequencies were obtained by system identification from the time domain response of the rotor subject to random excitation. The results are presented in Table 6. No lead-lag frequencies are reported, because no reference data are available for comparison. The first lead-lag frequency (rigid motion), due to a hinge offset of 0.23 m (9 in., $0.027R$), is 0.20Ω. Table 6 shows the results from the model with beam properties taken from Ref. [7], followed by the results obtained with the beam properties estimated by the present procedure. The agreement on the lower flap frequencies is quite good because they are dominated by the centrifugal stiffness. The fourth frequency obtained from our model is appreciably lower than in Ref. [7], due to the higher contribution of the structural stiffness to higher frequency flapping modes. The simplified, diagonal stiffness matrix used in Ref. [7] represents a first approximation of the true stiffness properties of the real beam. It can be useful for preliminary performance evaluation, but may cause underestimation of cross-coupling effects due to the anisotropy of the materials. The importance of the cross-coupling coefficients, in particular for the dynamics of composite rotor blades, was highlighted in [24]. The stiffness matrix reported in Table 5 shows significant couplings; some of them can be accounted for in a conventional beam analysis by applying offsets to the shear center or to the normal strain center, namely the couplings between twist and out-of-plane shear, or the couplings between axial force and in-plane bending. Other couplings are strongly related to the anisotropy of the material, namely the coupling between axial and out-of-plane shear forces, and that between axial force and twist. A simple hover simulation, with 4° of collective pitch, has been performed first with the properties from Ref. [7], then with properties from the proposed analysis. Both complete and "diagonalized", i.e. neglecting the coupling terms, situations were considered. A comparison of some significant results is shown in Table 7.

Table 6
Comparison of in vacuo rotating frequencies (1/rev)

Mode	AFC blade			Reference blade	
	MBDyn	MBDyn[a]	[7]	MBDyn	[7]
First flap	1.02	1.02	1.02	1.02	1.02
Second flap	2.59	2.58	2.62	2.61	2.62
Third flap	4.69	4.55	4.79	4.67	4.79
Fourth flap	7.31	6.89	7.85	7.20	7.85
First twist	3.31	3.38	3.38	6.48	6.16
Second twist	9.65	10.0	9.78	18.4	18.3

[a] Stiffness properties from beam-section analysis.

Table 7
Hover simulations with different stiffness properties

	Ref. [7]	Diagonal	Coupled
Tip vertical displacement (m)	0.3369	0.3370	0.3153
Flap at flap hinge (deg)	2.275	2.276	2.129
Elastic twist from root to tip (deg)	−0.006	−0.005	−0.120
Thrust (N)	2.277e4	2.284e4	2.183e4

7. Harmonic actuation

The effectiveness of the active twist of the rotor blade was investigated by performing analyses of the rotor in air with harmonic actuation of the blade. The hover condition was considered first. Root to tip twist and root flap angles due to harmonic actuation of the active twist blade are shown in Fig. 7 for the frequency range 0.25–10Ω. A voltage of 250 V was applied to the electrodes of the AFC, corresponding to an average electric field of 1300 V/mm (33,000 V/in). The frequency response shows a peak at about 3.5/rev corresponding to the first twist mode of the blade, that is only lightly damped by the aerodynamics. Another peak at about 2/rev results from the excitation of the first flexible flap mode of the blade, that resonates at a lower than expected frequency due to the high aerodynamic damping of the flap modes. The blade twist from Ref. [7] does

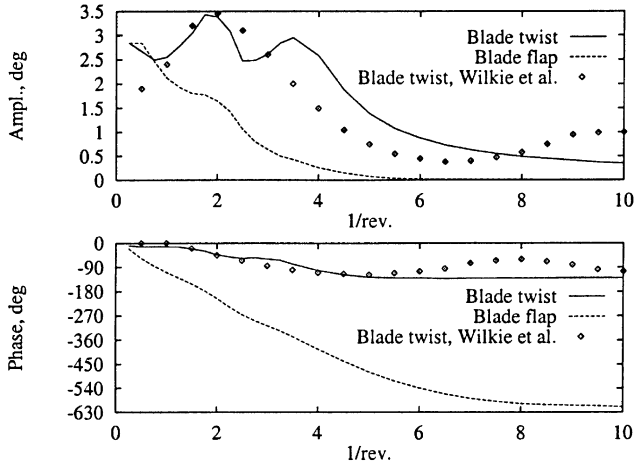

Fig. 7. Frequency response of root-to-tip twist and root flap at maximum control voltage.

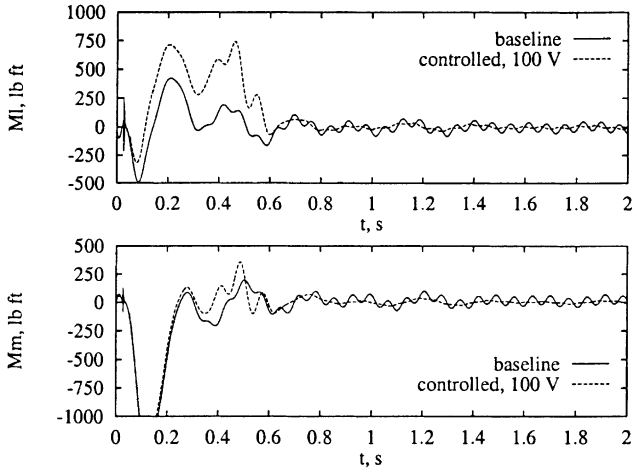

Fig. 8. Bending moments about x and y axes at the mast; advance ratio $\mu = 0.20$; voltage: 100 V (40% of allowable) at 2/rev; 131° phase shift.

show the peak at 2/rev, but there is no evidence of the first twist mode at about 3.5/rev (Fig. 7), possibly due to the unsteady aerodynamics model used in the mentioned reference, that adds considerable aerodynamic damping to the pitch movement. In the present work, structural damping is the main source of damping for the pitch movement. The frequency response of the thrust (not shown) showed a peak at zero frequency, due to the steady change in pitch, and the two peaks at 2/rev and 3.5/rev mentioned above. The thrust is nearly zero at 1.02/rev, because at the first, rigid flap frequency, all the work made by the aerodynamic forces is spent in rigidly flapping the blades at blade rigid flapping resonance.

A primary goal for the active control of rotorcraft by controlling the pitch of the blades is to obtain an induced twist of the order of 2° in the range of 0–5Ω [7,25]; Fig. 7 clearly shows that the goal is achievable.

Forward flight conditions at different advance ratios have been subsequently considered; open-loop 2/rev actuation has been performed with the objective of reducing the vibrations at the mast induced by the steady forward flight. These vibrations mainly are 4/rev due to the periodic forces generated by the four blades of the rotor; they can be canceled by using 2/rev actuation since 2/rev pitch change causes 2/rev flapping of the rotor, which in turn results in Coriolis forces in the plane of the rotor at twice the frequency of the flapping motion. Open loop control results are reported in Figs. 8–10 at different advance ratios ranging from 0.20 to 0.30. Convergence at higher advance ratios is difficult.

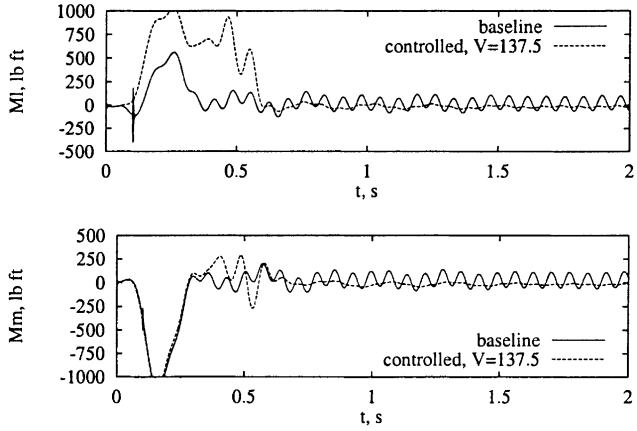

Fig. 9. Bending moments about x and y axes at the mast; advance ratio $\mu = 0.25$; voltage: 137.5 V (55% of allowable) at 2/rev; 128° phase shift.

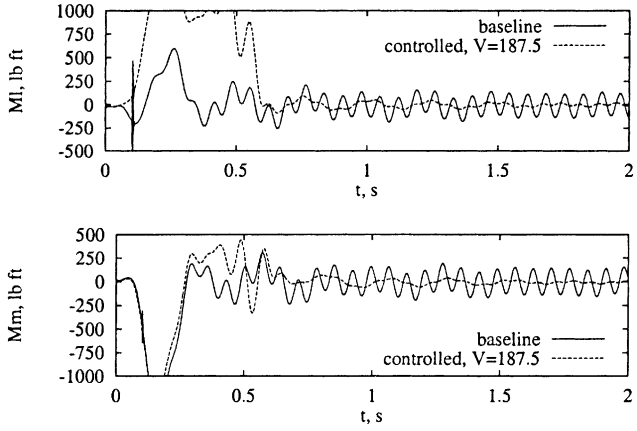

Fig. 10. Bending moments about x and y axes at the mast; advance ratio $\mu = 0.30$; voltage: 187.5 V (75% of allowable) at 2/rev; 127° phase shift.

8. Conclusions

An approach to the analysis of complex dynamic systems, like helicopter rotors in the presence of dis-

tributed active control, has been depicted. It connects several advanced tools for the structural characterization of the system at different levels. A formulation for blade section characterization with embedded piezoelectric devices has been established. It has been used to determine the stiffness and piezoelectric properties of the blade of an active twist rotor analytical model. A procedure based on FEA has been used to characterize the active fiber composite piezoelectric material with interdigitated electrodes that is required to obtain in-plane anisotropic strain induction, and thus rotor blade twist induction. Multibody analysis was used to investigate the behavior of an active twist rotor in vibration suppression by open- and close-loop controls in the frame of a global modeling approach. Partial results on the ability of the active twisting in reducing the airloads transmitted by the rotor have been illustrated. The predicted properties of the AFC blade show good agreement with available analytical data, and moreover they give a deeper insight into the properties of a composite piezoelectric beam in terms of stiffness cross-couplings. The proposed approach to the analysis of actively twisted rotor blades is able to analyze the complex operating conditions of an actively controlled rotorcraft to a comparatively high degree of refinement. The active twisting of the blade represents an interesting and very promising means for the active control of the dynamics of a rotor.

References

[1] ANSI/IEEE, IEEE standard on piezoelectricity. Tech Report IEEE176-78, IEEE, September 29, 1978.

[2] Bent AA, Hagood NW, Rodgers JP. Anisotropic actuation with piezoelectric fiber composites. J Intell Mat Syst Struct 1995;6:338–49.

[3] Hagood NW, Kindel R, Ghandi K, Gaudenzi P. Improving transverse actuation of piezoceramics using interdigitated surface electrodes. In: SPIE Smart Structures and Materials Conference, February 1–4, vol. 1917(1), 1993. p. 341–52.

[4] Chen T. Micromechanical estimates of the overall thermoelectroelastic moduli of multiphase fibrous composites. Int J Solids Struct 1994;31(22):3099–111.

[5] Dunn ML, Taya M. Micromechanics predictions of the effective electroelastic moduli of piezoelectric composites. Int J Solids Struct 1993;30(2):161–75.

[6] Dunn ML. A theoretical framework for the analysis of thermo-electroelastic heterogeneous media with applications. J Intell Mat Syst Struct 1995;6:255–65.

[7] Wilkie WK, Park KC, Belvin WK. Helicopter dynamic stall suppression using piezoelectric active fiber composite rotor blades. In: AIAA/ASME/AHS Structures, Structural Dynamics and Materials Conference, April 20–23, 1998; Long Beach, CA. AIAA-98-2002.

[8] Rodgers JP, Hagood NW. Preliminary mach-scale hover testing of an integral twist-actuated rotor blade. In: SPIE Conference, March 1–5, 1998; San Diego, CA.

[9] Janos BZ, Hagood NW. Overview of active fiber composites technologies. In: Proceedings of the Sixth International Conference on new Actuators – ACTUATOR98, June, 1998; Bremen, Germany.

[10] Carpenter MJ. Using energy methods to derive beam finite elements incorporating piezo-electric materials. J Intell Mat Syst Struct 1997;1.

[11] Cesnik C, Shin S. Structural analysis for designing rotor blades with integral actuators. In: Proceedings of 39th AIAA Structures, Structural Dynamics and Materials Conferences, 1998; Long Beach. AIAA-98-2107.

[12] Giavotto V, Borri M, Mantegazza P, Ghiringhelli GL, Caramaschi V, Maffioli GC, Mussi F. Anisotropic beam theory and applications. Comput Struct 1983;16(1–4):403–13.

[13] Ghiringhelli GL, Mantegazza P. Linear, straight and untwisted anisotropic beam section properties from solid finite elements. Compos Engrg 1994;4(12):1225–39.

[14] Ghiringhelli GL, Mantegazza P, Masarati P. Numerical modelling of anisotropic non homogeneous beams with embedded piezoelectric sensors and actuators. In: Proceedings of the Seventh International Conference on Adaptive Structures and Technologies, September 23–25, 1996; Rome, Italy.

[15] Ghiringhelli GL, Masarati P, Mantegazza P. Characterisation of anisotropic, non-homogeneous beam sections with embedded piezo-electric materials. J Intell Mat Syst Struct 1997;8:842–58.

[16] Masarati P. Comprehensive multibody aeroservoelastic analysis of integrated rotorcraft active controls. PhD Thesis, Dipartimento di Ingegneria Aerospaziale, Politecnico di Milano, Milano, Italy,1999.

[17] Masarati P, Mantegazza P. On the discretisation C^0 of beams by finite elements and finite volumes. l'Aerotecnica Missili e Spazio 1997;75:77–86.

[18] Ghiringhelli GL, Masarati P, Mantegazza P, Nixon MW. Multibody analysis of a tiltrotor configuration. Nonlinear Dyn 1999;19:333–57.

[19] Ghiringhelli GL, Masarati P, Mantegazza P. A multi-body implementation of finite volume beams. AIAA J 2000;38:131–8.

[20] Pitt DM, Peters DA. Theoretical prediction of dynamic-inflow derivatives. Vertica 1981;5:21–34.

[21] Ghiringhelli GL, Masarati P, Mantegazza P. Multi-body aeroelastic analysis of smart rotor blades, actuated by means of piezoelectric devices. In: CEAS International Forum on Aeroelasticity and Structural Dynamics, vol. II, June 17–20, 1997; Rome, Italy. p. 115–22.

[22] Wilkie WK, Mirick PH, Langston CW. Rotating shake test and modal analysis of a model helicopter rotor blade. TM 4760, NASA, 1997.

[23] Wilkie WK, Wilbur ML, Mirick PH, Cesnik CES, Shin S. Aeroelastic analysis of the NASA/Army/MIT active twist rotor I. In: American Helicopter Society 55th Forum, May 25–27, 1999; Montreal, Canada.

[24] Ghiringhelli GL, Lanz M. Dynamic optimisation of bearingless helicopter rotors. In: CEAS International Forum on Aeroelasticity and Structural Dynamics, vol. III, June 17–20, 1997; Rome, Italy. p. 75–84.

[25] Giurgiutiu V, Chaudry Z, Rogers CA. Engineering feasibility of induced strain actuators for rotor blade active vibration control. J Intell Mat Syst Struct 1995;6:583–97.